Polarization-selective three-photon absorption and subsequent photoluminescence in $CsPbBr_3$ single crystal at room temperature

D. J. Clark,[1] C. C. Stoumpos,[2] F. O. Saouma,[1] M. G. Kanatzidis,[2] and J. I. Jang[1,*]

[1]*Department of Physics, Applied Physics and Astronomy, State University of New York (SUNY) at Binghamton, P.O. Box 6000, Binghamton, New York 13902 USA*

[2]*Department of Chemistry, Northwestern University, Evanston, Illinois 60208, USA*

(Received 22 February 2016; published 5 May 2016)

We report on highly polarization-selective three-photon absorption (3PA) in a Bridgman-grown single crystal of $CsPbBr_3$ oriented along the (112) direction, which is an inorganic counterpart to emerging organic-inorganic hybrid halide perovskites for solar-cell and optoelectronic applications. The crystal exhibits strong photoluminescence (PL) at room temperature as a direct consequence of 3PA of fundamental radiation. Interestingly, 3PA disappears when the input polarization is parallel to the (-110) direction. This 3PA effect is strongest when orthogonal to (-110) and the corresponding 3PA coefficient was measured to be $\gamma = 0.14 \pm 0.03$ cm^3/GW^2 under picosecond-pulse excitation at the fundamental wavelength of $\lambda = 1200$ nm. The laser-induced damage threshold was also determined to be about 20 GW/cm^2 at the same wavelength. Based on relative PL intensities upon λ tuning over the entire 3PA range (1100–1700 nm), we determined the nonlinear optical dispersion of the 3PA coefficient for $CsPbBr_3$, which is consistent with a theoretical prediction. Experimentally observed significant polarization dependence of γ was explained by relevant selection rules. The perovskite is potentially important for nonlinear optical applications owing to its highly efficient 3PA-induced PL response with a sharp on/off ratio by active polarization control.

DOI: 10.1103/PhysRevB.93.195202

I. INTRODUCTION

Recently, the research community has shown considerable interest in perovskite materials triggered by a remarkable breakthrough in the power conversion efficiency (PCE) for the direct conversion of sunlight into electricity [1–8]. Especially, organic-inorganic hybrid halide perovskites, ABX_3, (A^+ = organic cation, $B^{2+} = Sn^{2+}$ or Pb^{2+}, and $X^- = Br^-$ or I^-) have attracted significant interest for photovoltaic (PV) applications due to their high photon absorptivity, wide direct band gaps with superior charge transports, as well as their cost-effective methods of fabrication [9]. In particular, the hybrid perovskites $CH_3NH_3PbX_3$ ($MAPbX_3$) have been extensively studied as potential PV materials, and $MAPbX_3$-based PV cells have shown remarkable PCEs up to ~20% [8–12]. While the actual device architecture is a critical factor in terms of technology evolution, the basic understanding of essential light-matter interaction in these perovskite materials is unarguably important for increasing the PCE as well as discovering other emerging optoelectronic properties such as radiation detection [13], thermoelectricity [14], lasing [15], and light-emitting diodes [16].

Nonlinear optical (NLO) effects in these materials are relatively less explored but potentially important, and in fact they gained significant interest quite recently [17–19]. For example, some Ge-based hybrid iodides, $AGeI_3$, [$A^+ = MA^+$ or $HC(NH_2)_2^+ = FA^+$] exhibit strong "phase-matched" second harmonic generation (SHG) owing to their noncentrosymmetric crystal structure (*R3m*) [17]. Most remarkably, it was demonstrated that their SHG efficiencies are notably higher than those of the inorganic counterpart $CsGeI_3$ because of the additional polar character in the MA^+ and FA^+ cations oriented within the perovskite structure. Considering that NLO materials have been typically available from either solely organic or solely inorganic perspective, hybrid NLO materials such as the hybrid halide perovskites can provide unique opportunities since the combination of their organic-inorganic properties can be further exploited.

Typical hybrid halide perovskites show a large linear absorption coefficient near the band edge which can exceed 10^4 cm^{-1} [18]. Excellent linear optical absorption implies that they can be also efficiently excited by higher-order NLO absorption. For instance, Walters *et al.* have provided a study on the two-photon absorption (2PA) coefficient β of $MAPbBr_3$ that was reported as 8.6 cm/GW at the fundamental wavelength of $\lambda = 800$ nm under femtosecond-pulse excitation [18]. Reference [17] also indicates that $MAGeI_3$ is 2PA active at 1064 nm under picosecond-pulse excitation as confirmed by subsequent strong PL. The corresponding β value was measured to be 91.0 cm/GW with a saturable absorption intensity of 2.0 GW/cm^2 based on an order-of-magnitude estimate for the *powdered* sample. For comparison, conventional PV materials (E_g: band gap), specifically the inorganic binary semiconductors CdS ($E_g = 2.42$ eV) and CdSe ($E_g = 1.74$ eV), yield 2PA coefficients of 5.5 cm/GW ($\lambda = 532$ nm) and 18 cm/GW ($\lambda = 1064$ nm), respectively [20]. In fact, there have been many studies regarding the theoretical framework for multiphoton absorption (MPA) in semiconductors [21–23] as well as experimental investigations on the NLO absorption coefficients and NLO refractive indices in PV materials [24,25]. Current interest in MPA includes multiphoton spectroscopy and microscopy [26,27] and plasma physics via multiphoton ionization [28] as well as optical limiting applications [29].

In this paper, we present polarization-dependent three-photon absorption (3PA) and subsequent strong PL in a single crystal of the all-inorganic perovskite $CsPbBr_3$ at room

*jjoon@binghamton.edu

temperature by employing a recently developed wavelength-dependent Z-scan nonlinear spectroscopy (WDZNS) method [30]. The WDZNS technique is ideal for determining the relevant NLO dispersion because it can spectrally resolve NLO harmonic generation and PL as a function of input intensity as well as input wavelength, thereby enabling us to study coexisting NLO phenomena and the dynamics of excitonic matter. Therefore, we report on the wavelength-dependent 3PA coefficient $\gamma(\lambda)$ of $CsPbBr_3$ under picosecond-pulse excitation over its entire 3PA band. The experimental dispersion shows good agreement with a theoretical two-band model [22]. We also found that $CsPbBr_3$ has a very high laser-induced damage threshold of 20 GW/cm^2 at $\lambda = 1200$ nm, where the 3PA efficiency is characterized by $\gamma = 0.14 \pm 0.03$ cm^3/GW^2; this value is about two to three times higher than that for a semiconductor having a similar band gap [23]. We explained the sharp polarization dependence of $\gamma(\lambda)$ based on 3PA selection rules. Most of all, the perovskite is highly luminescent under efficient 3PA at room temperature with a clear-cut polarization contrast. Our results imply that $CsPbBr_3$ is potentially important for MPA-related NLO devices and applications.

II. SAMPLE PREPARATION

Raw $CsPbBr_3$ was prepared by reacting equimolar amounts of CsBr (4.26 g, 20 mmol) and $PbBr_2$ (7.34 g, 20 mmol) in a fused silica ampoule (12 mm OD, 10 mm ID) and flame sealed at 10^{-4} mbar vacuum. The ampoule was heated at 700 °C over 24 h, soaked there for 5 h, then the furnace was rocked for 2 h to ensure homogeneity of the melt, soaked for 2 h, and then slowly cooled to room temperature over 24 h.

The resulting opaque, dark-orange ingot was then crushed and transferred into a fused silica tube (9 mm OD, 7 mm ID) with a tapered end at the bottom to facilitate the crystal growth. As shown in Fig. 1(a), the crystal growth of a 7-mm-diameter crystal ingot was achieved in a vertical, three-zone Bridgman furnace, employing a translation speed of 10.0 mm/h for a set temperature profile, as reported previously [13]. The resulting transparent orange crystal was subsequently cut into 10-mm slices along the growth direction using a diamond blade saw and finely polished down to 1-μm smoothness using WD-40 as an abrasive medium [Fig. 1(b)]. The growth direction of our sample is (112) as determined by x-ray diffraction (see the Supplemental Material [31]). Detailed sample preparation and basic characterizations such as structural, thermal, linear optical, and electrical properties are described in Ref. [13].

$CsPbBr_3$ is centrosymmetric and crystalizes in the orthorhombic space group (*Pbnm*) undergoing two successive phase transitions from cubic (*Pm-3m*, above ~130 °C) to tetragonal (*P4/mbm*, between ~88 °C and 130 °C) and finally to orthorhombic below ~88 °C [32]. In the orthorhombic modification, $CsPbBr_3$ adopts a distorted perovskite structure where the octahedral $\{PbBr_6\}^{4-}$ building blocks undergo a significant degree of tilting with respect to the ideal cubic perovskite structure where all the octahedra are perfectly aligned (Pb-Br-Pb angle is strictly 180°). This octahedral complex embedded in the orthorhombic matrix of Cs^+ cation contributes significantly to optical properties of $CsPbBr_3$ [33]. Figure 1(c) shows the crystal structure of $CsPbBr_3$ viewed along the (112) direction [see Fig. S1(b) for the (001) direction].

$CsPbBr_3$ is a direct band-gap semiconductor with a band edge occurring at 2.25 eV (~550 nm) across the *R* point at room temperature as determined by optical absorption spectroscopy [Fig. 1(d)]. Primary optical transitions occur within the highest valence band (Γ_6^+) and the two lowest spin-orbit-split conduction bands (Γ_6^- and Γ_8^-). The associated energy level diagram and linear optical selection rules are discussed in Ref. [33]. The optical and electrical properties of the $CsPbBr_3$ specimen studied in these experiments have been tested as a crystal quality control and they were found to be in good agreement with previous reports ($E_g = 2.25$ eV, $\rho = 1.1 \times 10^9\ \Omega$ cm) [13].

III. EXPERIMENTAL METHODS

Our NLO experiments were performed at room temperature utilizing WDZNS [30]. Unlike a conventional Z-scan [34], WDZNS is available in both reflection and transmission geometry together with the spectral resolving capability to simultaneously monitor NLO and PL signals. The bulk $CsPbBr_3$ sample was loaded into a homemade sample holder that was mounted on a Z-scan translation stage. A train of 30-ps fundamental pulses was produced from an EKSPLA PG403 optical parametric oscillator (OPO), which was synchronously pumped by the frequency-tripled output (355 nm) from an EKSPLA PL-2250 series Nd:YAG laser with a repetition rate of 50 Hz. The laser-pulse energy from the OPO was adjusted to $E = 10\ \mu$J using a combination of a half-wave plate (HWP) and a linear polarizer (LP) before being focused

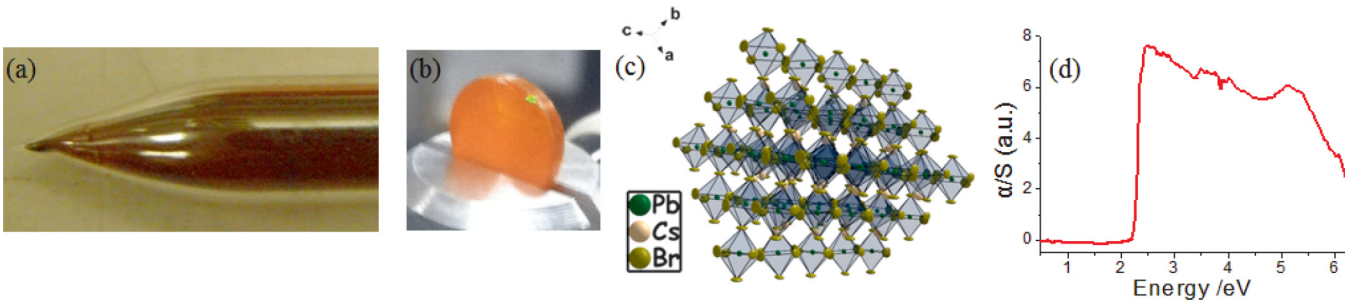

FIG. 1. (a) Bridgman-grown ingot of $CsPbBr_3$. (b) Polished $CsPbBr_3$ single crystal where 3PA-induced PL is clearly observed (bright green area near the edge) under IR excitation. (c) Crystal structure of $CsPbBr_3$ (*Pbnm*) viewed along the (112) direction. (d) UV-Vis-NIR absorption spectrum at room temperature.

onto the sample using a positive lens ($f = 7.5$ cm) with a spot size of ~200 μm in diameter. The corresponding sample position was far away from the Z-scan focus. Therefore, the change in the spot size was minimal when we varied the fundamental wavelength λ over a broad range [30]. In order to avoid reabsorption of optical signals by the sample having a macroscopic thickness (1.3 mm), harmonic generations as well as PL from the sample were collected in a reflection geometry to a fiber-optic bundle which was coupled to a selective-grating Horiba iHR320 spectrometer equipped with a charge-coupled device (CCD) camera. We confirmed that NLO harmonic signals from other optical components were negligible. The measured optical signals were calibrated with the known and measured λ-dependent efficiencies of all optical components. Any thermal load to the sample, which can potentially cause a transition to the tetragonal or cubic phase, is negligible basically due to the slow repetition rate of the laser.

The wavelength-dependent 3PA efficiency was compared by monitoring the resulting PL intensity as λ was tuned within the 3PA band with the input intensity I being kept constant, i.e., the same sample position Z; in this sense, the method is similar to PL excitation spectroscopy but it takes place under the 3PA condition. The PL method presented here also relies on the unique capability of WDZNS in which the input intensity can be varied in both λ and Z, namely, $I = I(\lambda, Z)$; the change in λ at a fixed Z first yields a relative NLO dispersion and a single Z-scan at a fixed λ will completely determine the *absolute* 3PA dispersion. However, we found that I^3 dependence of 3PA can result in optical damage at the focus during Z-scan, causing an incorrect estimation of γ. Therefore, we varied the input pulse energy at several selected $+Z$ positions (after the focus) outside the Rayleigh range to determine γ at $\lambda = 1200$ nm by monitoring the far-field transmittance of the fundamental beam using the CCD camera. The polarization dependence of 3PA along the (112) direction was also probed by monitoring the resulting PL counts when the polarization vector was rotated.

IV. RESULTS AND DISCUSSION

In fact, our initial interest on this material was more on accurate structural identification based on an SHG technique [35] that can sensitively provide a verdict regarding the presence or absence of an inversion center. The crystal symmetry is particularly important for perovskite-based PVs [36,37] because loss of the inversion symmetry can trigger ferroelectric polarization. The ferroelectric behavior of an active PV medium, in turn, can directly affect PCE of the PV device derived from the compound. However, we found that both second- and third-order harmonic signals were strongly masked by highly efficient PL triggered by fifth-order NLO absorption (3PA), which is the main focus of this work.

For example, Fig. 2 plots the optical response of $CsPbBr_3$ when λ was varied from 1700 to 1500 nm in steps of $\Delta\lambda = 100$ nm. Note that the spectral positions for SHG and third harmonic generation (THG) vary as a function of λ in accordance with $\lambda_{SHG} = \lambda/2$ and $\lambda_{THG} = \lambda/3$, respectively, whereas that for 3PA-induced PL remains the same since it involves the radiative recombination of charge carriers near the band gap [2.25 eV (550 nm)]. Figure 2(a) shows that the PL is very weak at $\lambda = 1700$ nm since this wavelength is below the onset of 3PA. The PL yield becomes stronger when tuning λ above the 3PA band edge due to its characteristic dispersion. We found that the spectral feature of the 3PA-induced PL is similar to the PL under typical one-photon absorption (1PA) at $\lambda = 355$ nm (see Supplemental Material [31]). Variations of the SHG and THG intensities as a function of λ seem to arise from the coherent interaction between NLO and fundamental radiation, i.e., spectral Maker fringe effects [38], but these NLO signals are relatively weak compared with the PL signal.

Interestingly, while $CsPbBr_3$ is known to be centrosymmetric (*Pbnm*), we found that our sample yields a nonzero SHG response, which is above the system background level. We confirmed that this SHG signal is from the sample, presumably arising from the sample surface or local symmetry-breaking effects in the bulk (defects or an intergrowth of centrosymmetric and noncentrosymmetric phases) assisted by the highly polarizable nature of the perovskite. This effect may cause a finite ferroelectricity especially when prepared into thin films [36,37]. However, we conclude that the compound is essentially centrosymmetric as clearly evidenced by much stronger THG over SHG throughout our experimental range, even when THG is being significantly reabsorbed by the

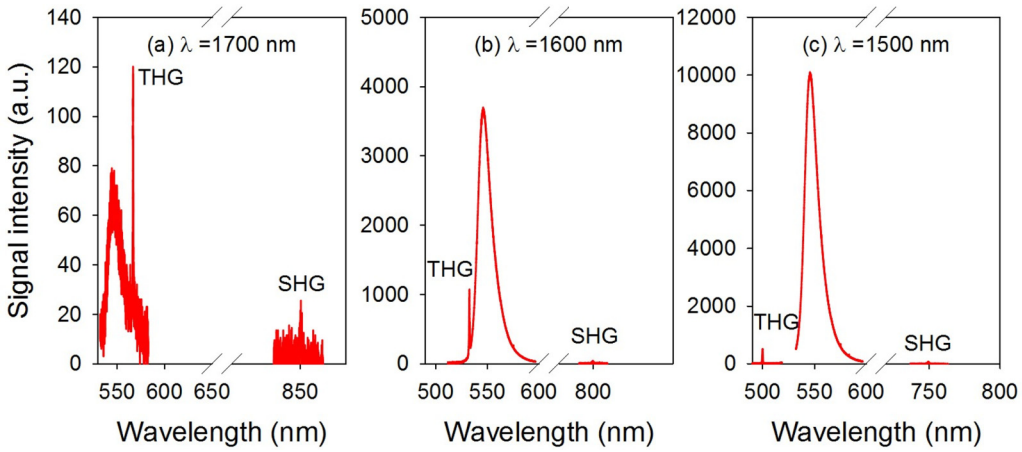

FIG. 2. NLO harmonic signals and 3PA-induced PL from $CsPbBr_3$ at (a) $\lambda = 1700$ nm, (b) $\lambda = 1600$ nm, and (c) $\lambda = 1500$ nm, respectively. The observed PL intensity strongly depends on λ due to the 3PA dispersion.

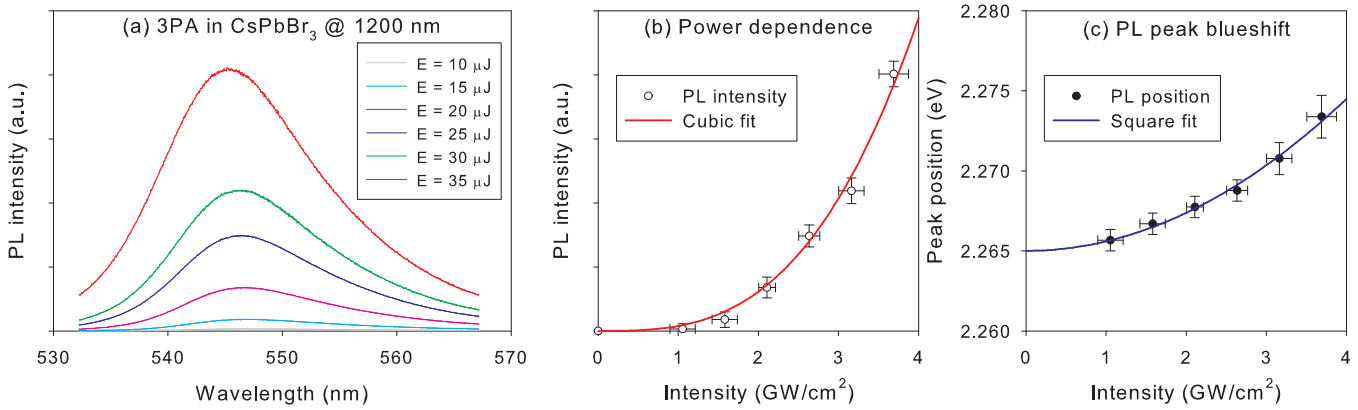

FIG. 3. (a) PL spectra at $\lambda = 1200$ nm for several excitation levels (10–35 μJ). (b) Intensity dependence of the PL (circles) fit by a cubic law (red). (c) Corresponding blue-shift of the PL (dots) fit by a square law (blue) based on the Burstein-Moss effect. Both I^3-dependent PL intensity and I^2-dependent PL blue-shift demonstrate the case of 3PA.

sample: As shown in Fig. 2, the THG photon energy is on or above the main PL band, whereas the SHG photon energy is below the band gap [39].

In order to confirm 3PA, the intensity dependence of the PL was measured at $\lambda = 1200$ nm. Figure 3(a) shows the series of PL spectra observed when the incident pulse energy was varied in the range of $E = 10-35$ μJ. We plot the corresponding PL intensities (circles) in Fig. 3(b) in terms of the input intensity. The red trace is a cubic fit to the observed data, clearly indicating the case for 3PA-induced PL. In Fig. 3(a), we also note that there is a noticeable blue-shift of the PL as the excitation level increases within our experimental range (see also Fig. S1). The dots in Fig. 3(c) show the spectral position of the PL maximum in energy units for each excitation level. The blue trace is a square fit, implying that the optical gap blue-shifts due to the band-filling effect in accordance with the Burstein-Moss shift [40]:

$$\Delta E_g = \frac{\hbar^2}{2m^*}(3\pi^2 n)^{2/3} = \frac{\hbar^2}{2m^*}(\pi^2 \tau \gamma I^3)^{2/3} \propto I^2, \qquad (1)$$

where $\hbar$ is the Planck constant, n is the density of photogenerated carriers, and m^* is the reduced effective mass of the bands associated with the optical transition. In Eq. (1), n is related to the 3PA generation rate, $G = n/\tau = \gamma I^3/3$, where $\tau = 30$ ps is the laser pulse width. In principle, the 3PA coefficient γ can be estimated based on the observed PL shift using Eq. (1). However, this requires time-resolved spectroscopy to precisely relate γ and ΔE_g because the effect is *transient* primarily induced by pulsed optical excitation. In fact, we found that the γ value inferred from the time-integrated PL data in Fig. 3 using theoretical m^* values [41,42] is several times smaller than the value from direct NLO experiments as detailed below. Density-dependent carrier relaxation dynamics and stimulated PL emission in $CsPbBr_3$ at cryogenic temperatures were studied under 1PA and available elsewhere [43].

Due to the associated NLO dispersion of the three-photon process, the 3PA efficiency depends on λ. For the process to occur, λ should lie in-between 1100 nm (2×550 nm) and 1650 nm (3×550 nm), where the former corresponds to the two-photon edge and the latter to the three-photon edge. Figure 4(a) plots the measured PL spectra when we varied λ from 1100 to 1700 nm, while keeping the input pulse energy a constant (22.5 μJ). We confirmed that the PL shape is unaltered upon wavelength tuning. In Fig. 4(b), we plot the corresponding PL intensities (dots) as a function of λ, together with excitation at $\lambda = 1000$ nm that indeed corresponds to 2PA. Note that there exist sharp increases in

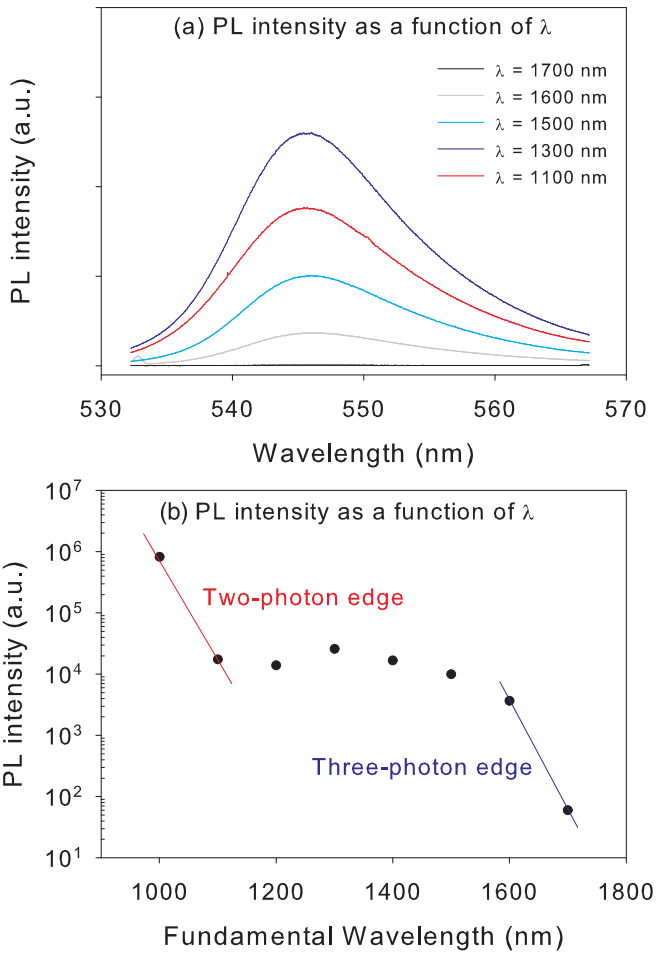

FIG. 4. (a) PL spectra under 3PA in our λ range. (b) Relative MPA efficiency as a function of λ in terms of the measured PL intensity. Both 2PA (red) and 3PA (blue) band edges are also shown.

the observed PL intensities when the order of MPA changes, i.e., λ is resonant with either the 2PA or 3PA edge, which is indeed consistent with their predicted spectral positions (colored lines for guidance). Clearly, the brightness of this wavelength-dependent PL is directly proportional to the carrier densities generated by the corresponding 3PA process, which in turn reflects the wavelength dependence of 3PA. The overall scaling factor can be determined by a single Z-scan at one wavelength to generate the absolute 3PA dispersion.

Because of possible sample damage as explained in Sec. III, however, Z-scan was not used to determine the absolute value of γ, which is proportional to the imaginary part of the fifth-order NLO tensor $\chi^{(5)}$ [34]. Instead, the transmitted fundamental beam at $\lambda = 1200$ nm was monitored for several fixed Z positions (for a consistency check). We varied the input pulse energy $E(\phi)$ over two orders of magnitude by the HWP-LP combination where ϕ is the HWP angle (see Supplemental Material [31]). First, the fundamental pulse energy $E_b(\phi)$ via sample transmittance was measured as a function of ϕ with a 5% neutral density (ND) filter *before* the sample, ensuring no 3PA. This linear transmittance can be used as a reference (see Fig. S3) for generating the normalized transmittance. With the ND filter *after* the sample, the transmitted energy in the nonlinear regime $E_a(\phi)$ was measured to determine γ where we varied ϕ starting from the lowest energy. Therefore, the ratio $E_a(\phi)/E_b(\phi)$ corresponds to the *normalized sample transmittance* and $E_a(\phi) = E_b(\phi)$ is expected if 3PA is insignificant. With increasing excitation level, however, efficient 3PA would cause a gradual transmission loss in $E_a(\phi)$.

Figure 5(a) plots E_b versus E_a at $\lambda = 1200$ nm for $Z = 0.286$ cm (red), 0.254 cm (blue), and 0.222 cm (pink), respectively, when $E(\phi)$ was varied from 0.2 to 21 μJ with the polarization vector $\hat{\mathbf{e}} = (l,m,n)$ parallel to the (11–1) direction; here the Fresnel transmittance $T = 82\%$ was taken into account at the incoming air-sample boundary (see Supplemental Material [31]). The corresponding intensity $I(\phi,Z)$ at the sample surface is given by

$$I(\phi,Z) = \frac{2P(\phi)}{\pi w^2(Z)} = \frac{2P(\phi)}{\pi w_0^2\left(1+Z^2/Z_0^2\right)}, \qquad (2)$$

where $P(\phi)$ is the input pulse power and $Z_0 = \pi w_0^2/\lambda \sim 0.15$ cm is the confocal parameter (Rayleigh range) with $w_0 \sim 24$ μm being the beam waist at $Z = 0$ calculated by $\sigma/f = \lambda/\pi w_0$ where $\sigma \sim 0.12$ cm is the measured Gaussian width of the incident beam. We found that sample damage occurs at $Z = 0.222$ cm, when the pulse energy exceeds 18 μJ as indicated by the arrow in Fig. 5(a). The laser-induced damage threshold (LIDT) of $CsPbBr_3$ at 1200 nm is therefore about 20 GW/cm^2 according to Eq. (2) for picosecond-pulse excitation. This LIDT value seems considerably higher than those for hybrid halide compounds $AGeI_3$ [17]. However, the damage mechanism for the current case is higher-order 3PA, whereas optical damage in $AGeI_3$ arises due to much more efficient 2PA.

By solving the equation for 3PA-induced light attenuation throughout an effective thickness d_{eff}, the normalized transmittance for 3PA is given by

$$\frac{E_a(\phi,Z)}{E_b(\phi,Z)} = \frac{2}{\pi^{1/2}p}\int_0^\infty \ln\left[\sqrt{1+p^2e^{-2x^2}} + pe^{-x^2}\right]dx, \qquad (3)$$

where the dimensionless parameter p is defined by $p(\phi,Z) \equiv (2\gamma d_{\text{eff}})^{1/2} I(\phi,Z)$ [25], and the effective thickness of the sample is $d_{\text{eff}} \simeq 0.04$ cm (see Supplemental Material [31]). The colored traces in Fig. 5(a) are fits generated by numerically evaluating Eq. (3) with only one adjustable parameter $\gamma = 0.14$ cm^3/GW^2 that explains the three experimental data sets *simultaneously*. The corresponding error-bar range for the γ value is about 20%.

The fifth-order NLO dispersion of the 3PA coefficient, i.e., its wavelength dependence, is well known from a simple

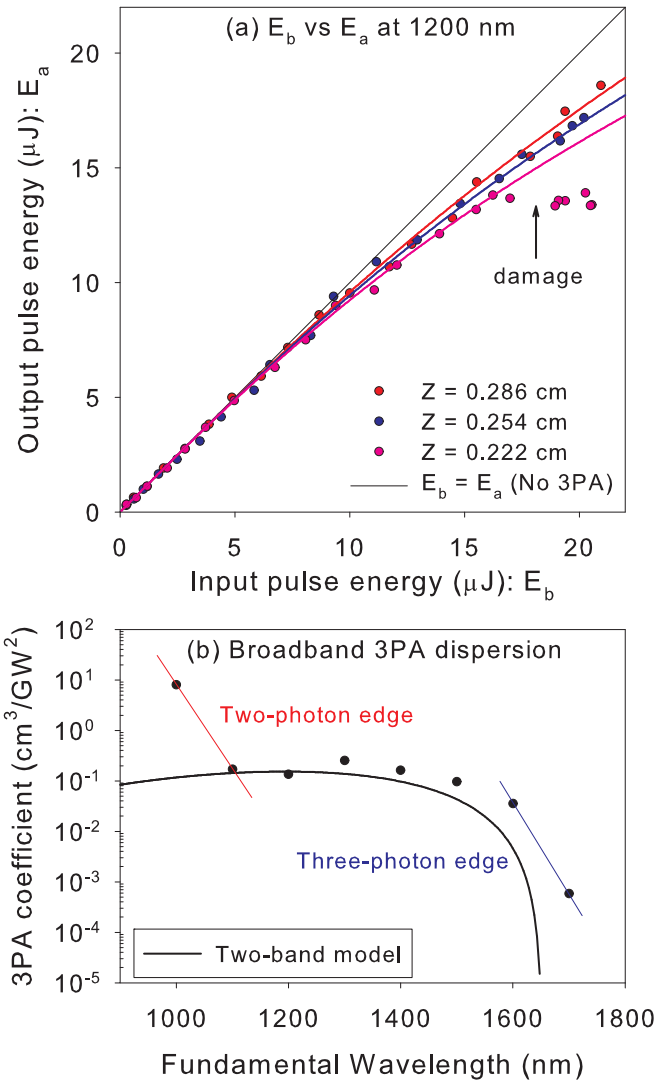

FIG. 5. (a) E_b vs E_a at several Z values (colored dots), superimposed by fits (colored curves) with a single fit parameter of $\gamma = 0.14$ cm^3/GW^2 for $\hat{\mathbf{e}}$ along the (11–1) direction. The solid line corresponds to the case of no 3PA. (b) $\gamma(\lambda)$ determined by PL-based WDZNS (dots). The solid curve corresponds to a theoretical two-band model scaled up by a factor of 3 to fit the data.

two-band model [22]:

$$\gamma(x) = \frac{2^{9/2}3^{10}\pi^2}{5}\left(\frac{e^2}{\hbar c}\right)^3 \hbar^5 S_3 \frac{(3x-1)^{5/2}}{(3x)^9}, \quad (4)$$

where $e^2/\hbar c$ is the fine-structure constant, $x = E/E_g = [(hc/\lambda)/E_g]$ is the dimensionless dispersion parameter, and $S_3 = (\frac{p_{vc}}{m_e})^2 m^{*7/2}/(m_c^4 n_0^3 E_g^{13/2})$ with m_e, m_c, and m^* being the bare electron mass, effective mass of the conduction band, and the reduced effective mass incorporating both conduction and valence bands, respectively. Note that in Eq. (4) the scaling of γ for different materials is solely determined by S_3, whereas the wavelength dependence arises from x. The dipole matrix element p_{vc} in S_3 is proportional to (i) the joint density of states in the band overlap integral and (ii) the dipole oscillator strength, and can be estimated by band-structure calculations. Theoretical calculations yield $S_3 = \eta m^{*5/2}/(m_c^4 n_0^3 E_g^{11/2})$, where η is a model-dependent numerical factor; for example, $\eta = \frac{1}{4}$ by a $\mathbf{k}\cdot\mathbf{p}$ perturbation theory or $\frac{3}{4}$ by a Hartree-Fock calculation, but η can be larger by an order of magnitude depending on approximation methods for evaluating p_{vc} [22,23,25].

Rather than relying on a specific calculation of p_{vc}, we therefore compared the theoretical γ value of $CsPbBr_3$ with an *experimental* reference value of $\gamma' = 0.007$ cm^3/GW^2 of ZnO at $x = 0.46$ [25], thereby eliminating the free factor η in S_3:

$$\frac{\gamma}{\gamma'} = \frac{S_3}{S_3'} = \left(\frac{m^*}{m^{*\prime}}\right)^{5/2}\left(\frac{m_c'}{m_c}\right)^4\left(\frac{n_0'}{n_0}\right)^3\left(\frac{E_g'}{E_g}\right)^{11/2} \simeq 7.34, \quad (5)$$

where we used the primed band parameters for ZnO from Ref. [44] and those for $CsPbBr_3$ from $m^* = 0.073m_e$ and $m_c = 0.15m_e$ [42], $E_g = 2.25$ eV, and $n_0 = 2.45$. Therefore, our theoretical calculation based on Eq. (5) yields $\gamma = 0.007$ cm^3/GW^2 $\times$ 7.34 $\simeq$ 0.051 cm^3/GW^2, which explains our experimentally determined $\gamma = 0.14 \pm 0.03$ cm^3/GW^2 at 1200 nm ($x = 0.46$) within a factor of 3. In Fig. 5(b), we plot the theoretical NLO dispersion of $\gamma(\lambda)$ (solid curve) from Eqs. (4) and (5), overlaid with experimental wavelength-dependent 3PA coefficients (dots) determined by our PL-based WDZNS technique. The difference between the model and the experimental data near the 3PA band edge (blue line) could be due to 3PA in Urbach tailing below the band gap and/or four-photon excitation.

3PA selection rules for centrosymmetric $CsPbBr_3$ with orthorhombic symmetry (D_{2h}) are closely related to those for a higher-symmetry point group (O_h), but extra dynamical parameters are required, which should be determined experimentally in general [45,46]. In $CsPbBr_3$, only Γ_4^- and Γ_5^- transitions are allowed by 3PA, where the associated bands and corresponding polarization dependencies are detailed in the Supplemental Material [31] for our excitation geometry, i.e., when the beam propagates along the (112) direction of the sample. In order to study the polarization dependence of γ experimentally, we monitored the relative PL intensities as a function of ϕ without the LP; rotating the HWP by ϕ therefore simply rotates the polarization vector by $2\phi \equiv \theta$ (Fig. 6). This PL method correctly reflects polarization-dependent γ because we confirmed that the PL is essentially unpolarized.

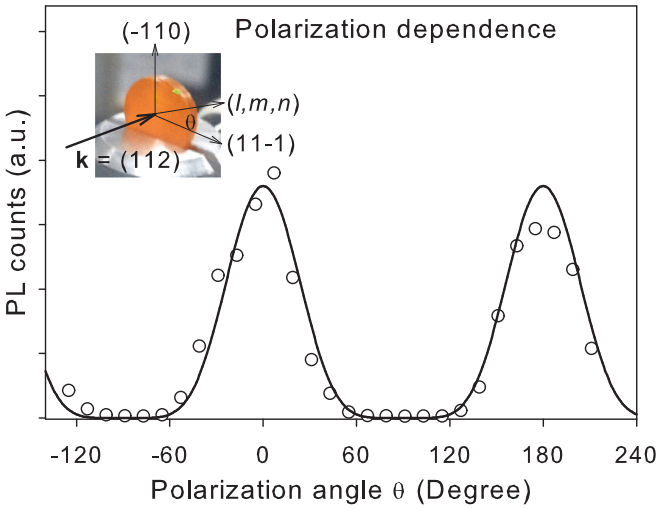

FIG. 6. Polarization dependence of 3PA at $\lambda = 1200$ nm along the (112) direction, showing strongest 3PA with $\hat{\mathbf{e}}$ parallel to (11–1).

It is predicted that the PL method yields a much clearer polarization contrast, when compared with direct monitoring of fundamental absorption. We confirmed that the two methods indeed yielded consistent results (see Fig. S6 for the latter method).

Figure 6 plots the polarization dependence of γ (circles) as probed by the 3PA-induced PL response as a function of θ. Interestingly, we found that 3PA is highly forbidden when the polarization vector is parallel to the twofold (−110) direction. As discussed in the Supplemental Material [31], the experimental polarization dependence can be explained by the Γ_4^- transition with a negligible contribution from $\Gamma_6^+ \otimes \Gamma_8^-$ [47]. The corresponding polarization dependence in the D_{2h} space group can be written as $\mu l^6 + \nu m^6 + n^6$ where μ and ν are additional dynamical parameters introduced due to the actual asymmetry of the orthorhombic phase. We found that $\mu = \nu = 0$ best explains our experimental observation with the $\cos^6\theta$ dependence for our excitation geometry, as indicated by the solid trace in Fig. 6.

V. CONCLUDING REMARKS

In conclusion, $CsPbBr_3$ proves to be a versatile semiconductor in which various NLO phenomena coexist under intense electromagnetic perturbation. Although the harmonic generation efficiency is relatively weak, the perovskite exhibits a very strong PL via efficient NLO absorption where the corresponding 3PA coefficient was measured to be $\gamma = 0.14 \pm 0.03$ cm^3/GW^2 at 1200 nm, together with wavelength and polarization dependence. This γ value is two to three times larger than those of conventional semiconductors with similar band gaps such as GaP and CdS [23]. It should be noted that 3PA-active materials are not necessarily luminescent under 3PA especially at room temperature; for example, the 3PA-induced PL in CdS is sufficiently bright only at cryogenic temperatures [48,49]. Our study confirms the excellent PL response of the title compound from the perspective of nonlinear optics, which may provide useful information on the nature of the excited states and the future design of this class of materials

for photovoltaic and light-emitting device applications. Highly luminescent materials with a large LIDT value as well as a sharp on/off ratio under IR illumination at room temperature are also ideal for MPA-based sensing and imaging especially when available through cost-effective fabrication. Future work is aimed toward measuring MPA efficiencies and PL yields for hybrid halide perovskites within band-gap engineering, which is predicted to significantly affect all the NLO efficiencies. Currently, we are also investigating time-resolved measurements of the PL under "resonant" 2PA or 3PA pumping, which can selectively create excitonic matter. Unlike conventional 1PA which initially generates hot charge carriers, the proposed NLO excitation method can be potentially utilized for studying relaxation dynamics of neutral excitons, which are selectively created by resonant MPA. The results will be reported elsewhere.

ACKNOWLEDGMENTS

The work was supported by Grant No. SC0012541 from the U. S. Department of Energy, Office of Science. We appreciate initial work by C. M. Harrison.

[1] I. Chung, B. Lee, J. He, R. P. H. Chang, and M. G. Kanatzidis, Nature (London) **485**, 486 (2012).
[2] M. M. Lee, J. Teuscher, T. Miyasaka, T. N. Murakami, and H. J. Snaith, Science **338**, 643 (2012).
[3] J. Burschka, N. Pellet, S.-J. Moon, R. Humphry-Baker, P. Gao, M. K. Nazeeruddin, and M. Grätzel, Nature (London) **499**, 316 (2013).
[4] M. Liu, M. B. Johnston, and H. J. Snaith, Nature (London) **501**, 395 (2013).
[5] I. Grinberg, D. V. West, M. Torres, G. Gou, D. M. Stein, L. Wu, G. Chen, E. M. Gallo, A. R. Akbashev, P. K. Davies, J. E. Spanier, and A. M. Rappe, Nature (London) **503**, 509 (2013).
[6] P. Gao, M. Grätzel, and M. K. Nazeeruddin, Energy Environ. Sci. **7**, 2448 (2014).
[7] J. You, Z. Hong, Y. M. Yang, Q. Chen, M. Cai, T.-B. Song, C.-C. Chen, S. Lu, Y. Liu, H. Zhou, and Y. Yang, ACS Nano **8**, 1674 (2014).
[8] N. J. Jeon, J. H. Noh, W. S. Yang, Y. C. Kim, S. Ryu, J. Seo, and S. I. Seok, Nature (London) **517**, 476 (2015).
[9] A. K. Chilvery, A. K. Batra, B. Yang, K. Xiao, P. Guggilla, M. D. Aggarwal, R. Surabhi, R. B. Lal, J. R. Currie, and B. G. Penn, J. Photon. Energy **5**, 057402 (2015).
[10] G. E. Eperon, S. D. Stranks, C. Menelaou, M. B. Johnston, L. M. Herz, and H. J. Snaith, Energy Environ. Sci. **7**, 982 (2014).
[11] W. Kong, Z. Ye, Z. Qi, B. Zhang, M. Wang, A. Rahimi-Iman, and H. Wu, Phys. Chem. Chem. Phys. **17**, 16405 (2015).
[12] H. Zhou, Q. Chen, G. Li, S. Luo, T.-b. Song, H.-S. Duan, Z. Hong, J. You, Y. Liu, and Y. Yang, Science **345**, 542 (2014).
[13] C. C. Stoumpos, C. D. Malliakas, J. A. Peters, Z. Liu, M. Sebastian, J. Im, T. C. Chasapis, A. C. Wibowo, D. Y. Chung, A. J. Freeman, B. W. Wessels, and M. G. Kanatzidis, Cryst. Growth. Des. **13**, 2722 (2013).
[14] Y. He and G. Galli, Chem. Mater. **26**, 5394 (2014).
[15] G. Xing, N. Mathews, S. S. Lim, N. Yantara, X. Liu, D. Sabba, M. Grätzel, S. Mhaisalkar, and T. C. Sum, Nat. Mater. **13**, 476 (2014).
[16] Z.-K. Tan, R. S. Moghaddam, M. L. Lai, P. Docampo, R. Higler, F. Deschler, M. Price, A. Sadhanala, L. M. Pazos, D. Credgington, F. Hanusch, T. Bein, H. J. Snaith, and R. H. Friend, Nat. Nanotechnol. **9**, 687 (2014).
[17] C. C. Stoumpos, L. Frazer, D. J. Clark, Y. S. Kim, S. H. Rhim, A. J. Freeman, J. B. Ketterson, J. I. Jang, and M. G. Kanatzidis, J. Am. Chem. Soc. **137**, 6804 (2015).
[18] G. Walters, B. R. Sutherland, S. Hoogland, D. Shi, R. Comin, D. P. Sellan, O. M. Bakr, and E. H. Sargent, ACS Nano **9**, 9340 (2015).
[19] Y. Wang, X. Li, X. Zhao, L. Xiao, H. Zeng, and H. Sun, Nano Lett. **16**, 448 (2016).
[20] E. W. V. Stryland, M. A. Woodall, H. Vanherzeele, and M. J. Soileau, Opt. Lett. **10**, 490 (1985).
[21] X. Feng, G. Xiong, X. Zhang, and H. Jiang, J. Phys.: Condens. Matter **20**, 025219 (2008).
[22] H. S. Brandi and C. B. de Araujos, J. Phys. C: Solid State Phys. **16**, 5929 (1983).
[23] V. Nathan, A. H. Cuenther, and S. S. Mitra, J. Opt. Soc. Am. B **2**, 294 (1985).
[24] Y.-P. Chan, J.-H. Lin, C.-C. Hsu, and W.-F. Hsieh, Opt. Express **16**, 19900 (2008).
[25] J. He, Y. Qu, H. Li, J. Mi, and W. Ji, Opt. Express **13**, 9235 (2005).
[26] W. R. Zipfel, R. M. Williams, and W. W. Webb, Nat. Biotechnol. **21**, 1369 (2003).
[27] C. Xu and W. W. Webb, in *Topics in Fluorescence Spectroscopy*, Vol. 5, edited by J. R. Lakowicz (Springer, New York, 2002), pp. 471–540.
[28] J. Kasparian and J.-P. Wolf, Opt. Express **16**, 466 (2008).
[29] P. Yang, J. Xu, J. Ballato, R. W. Schwartz, and D. L. Carroll, Appl. Phys. Lett. **80**, 3394 (2002).
[30] J. I. Jang, S. Park, D. J. Clark, F. O. Saouma, D. Lombardo, C. M. Harrison, and B. Shim, J. Opt. Soc. Am. B **30**, 2292 (2013).
[31] See Supplemental Material at http://link.aps.org/supplemental/10.1103/PhysRevB.93.195202 for (i) x-ray diffraction, (ii) typical room-temperature PL spectra under 1PA, 2PA, and 3PA, (iii) technical detail for pulse-energy tuning, and (iv) polarization-dependent optical properties of $CsPbBr_3$.
[32] S. Hirotsu, J. Harada, M. Iizumi, and K. Gesi, J. Phys. Soc. Jpn. **37**, 1393 (1974).
[33] S. Kondo, Phys. Status Solidi A **171**, 501 (1999).
[34] M. Sheik-Bahae, A. Said, T.-H. Wei, D. Hagan, and E. Van Stryland, IEEE J. Quantum Electron. **26**, 760 (1990).
[35] D. B. Hollis, Am. Mineral. **73**, 701 (1988).
[36] Y. Kutes, L. Ye, Y. Zhou, S. Pang, B. D. Huey, and N. P. Padture, J. Phys. Chem. Lett. **5**, 3335 (2014).
[37] Z. Fan, J. Xiao, K. Sun, L. Chen, Y. Hu, J. Ouyang, K. P. Ong, K. Zeng, and J. Wang, J. Phys. Chem. Lett. **6**, 1155 (2015).
[38] A. Zappettini, S. Pietralunga, A. Milani, D. Piccinin, M. Fere, and M. Martinelli, J. Electron. Mater. **30**, 738 (2001).

[39] No significant resonance effect was observed when THG overlaps with the main PL band.
[40] J. S. Manser and P. V. Kamat, Nat. Photonics **8**, 737 (2014)
[41] Y. H. Chang, C. H. Park, and K. Matsuishi, J. Korean Phys. Soc. **44**, 889 (2004).
[42] L. Protesescu, S. Yakunin, M. I. Bodnarchuk, F. Krieg, R. Caputo, C. H. Hendon, R. X. Yang, A. Walsh, and M. V. Kovalenko, Nano Lett. **15**, 3692 (2015).
[43] S. Kondo, T. Saito, H. Asada, and H. Nakagawa, Mater. Sci. Eng. B **137**, 156 (2007).
[44] H. Morkoç and Ü. Özgur, *General Properties of ZnO, in Zinc Oxide: Fundamentals, Materials and Device Technology* (Wiley, Weinheim, 2009).
[45] T. R. Bader and A. Gold, Phys. Rev. **171**, 997 (1968).
[46] A. Pasquarello and A. Quattropani, Phys. Rev. B **43**, 3837 (1991).
[47] A. Pasquarello and L. C. Andreani, Phys. Rev. B **41**, 12230 (1990).
[48] I. M. Catalano, A. Cingolani, and A. Minafra, Opt. Commun. **11**, 254 (1974).
[49] A. Penzkofer and W. Falkenstein, Opt. Commun. **16**, 247 (1976).